Sustainable Energy & Fuels

Ba1-xSrxFeO3-δ as an Improved Oxygen Storage Material for Chemical Looping Air Separation: A Computational and Experimental Study

Journal:	*Sustainable Energy & Fuels*
Manuscript ID	SE-ART-10-2024-001440.R1
Article Type:	Paper
Date Submitted by the Author:	27-Feb-2025
Complete List of Authors:	Acharya, Shree Ram; National Energy Technology Laboratory, Materials Science and Engineering; Leidos Inc, Climate, Energy and Environment Division Popczun, Eric; National Energy Technology Laboratory; Leidos Inc Paudel, Hari; National Energy Technology Laboratory, Functional Materials Engineering ; Leidos Inc Natesakhawat, Sittichai; National Energy Technology Laboratory; Leidos Inc Lekse, Jonathan; National Energy Technology Laboratory Duan, Yuhua; National Energy Technology Laboratory, United States Department of Energy

ARTICLE

$Ba_{1-x}Sr_xFeO_{3-\delta}$ as an Improved Oxygen Storage Material for Chemical Looping Air Separation: A Computational and Experimental Study

Received 30th September 2024,
Accepted 00th February 20xx

DOI: 10.1039/x0xx00000x

Shree Ram Acharya*[a,b]; Eric J. Popczun[a,b]; Hari P. Paudel[a,b]; Sittichai Natesakhawat[a,b]; Jonathan W. Lekse[a]; Yuhua Duan[a]

Chemical looping air separation (CLAS) is a promising technology to generate oxygen-rich gas streams to enable efficient carbon dioxide capture during fossil fuel combustion or gasification. CLAS relies on the capture and release of oxygen from the atmosphere using the redox properties of an oxygen-selective solid oxide carrier. This study investigates the redox characteristics of $Ba_{1-x}Sr_xFeO_{3-\delta}$ ($0.0 \le x \le 0.417$, $0.0 \le \delta \le 0.5$) using a combination of density functional theory (DFT) calculations and experimental verification using X-ray diffraction, thermogravimetric analysis, and oxygen-temperature-programmed desorption. The DFT computed energies of the $Ba_{1-x}Sr_xFeO_{3-\delta}$ perovskites reveal a composition-dependent transition from hexagonal to cubic phases as Sr-concentration or oxygen vacancy concentration increases. Oxygen vacancy formation energies of the cubic perovskites are found to be lower than their hexagonal counterparts. A low oxygen diffusion barrier of ~1 eV combined with the thermodynamic preference of $Ba_{1-x}Sr_xFeO_{3-\delta}$ compositions that form in a cubic phase suggest them as promising candidates for oxygen storage applications. Experimental results corroborate this finding by identifying $Ba_{0.75}Sr_{0.25}FeO_{3-\delta}$ at cubic phase as an optimal composition offering low-temperature oxygen storage capacities comparable to that of the state-of-art $Sr_{0.75}Ca_{0.25}FeO_{3-\delta}$ perovskite oxygen storage material at 325 °C and 350 °C.

Introduction

Despite the rapid development of novel energy sources such as solar, wind, nuclear, and biomass combustion in recent years[1], fossil fuels will continue to contribute to the energy market in short term[2]. Since the concentration of atmospheric carbon-dioxide (CO_2) emitted from fossil fuel combustion is significantly correlated with global climate change[3], its reduction is crucial to mitigate the currently increased wildfire, high heat waves, temperature cycle shifts, and other adverse environmental effects.

Oxygen-blown gasification offers an attractive alternative to both combustion and air-blown gasification as the resulting increase in partial pressure of CO_2 enhances its capture efficiency, affordability[4], and conversion into useful synthetic fuel products[5]. Pure O_2 or O_2-rich streams are required for this process. However, modern O_2 production technologies have various drawbacks when applied towards gasification. For example, cryogenic air separation is the most commonly used industrial-scale O_2 production technology, but it requires considerable capital cost and high energy input of 200-240 kWh/tonne-O_2[6,7] that limits its feasibility at modular scales. Other modular scale compatible methods have different downsides. For example, membrane separation[8] requires high temperatures and suffers from membrane instability[9], and zeolite-based pressure-/temperature-swing adsorption needs frequent regeneration and large operational volume[10]. Chemical looping air separation (CLAS)[11–13] is an emerging energy-efficient technology that mitigates these issues by using a metal oxide compound as an oxygen storage material (OSM) to selectively up take oxygen from air and then release it as an oxygen-rich stream. The OSM is reduced into an oxygen-depleted metal oxide through oxygen release and/or transport, while the reduced OSM can be re-oxidized by absorbing oxygen from air. Reduction in this process is typically endothermic while oxidation is exothermic. Overall, this process requires a minimum energy only about 60 kWh/tonne-O_2[14,15] making it attractive for modular implementation. The efficiency of the CLAS process is dictated by the redox performance and the stability of the OSM[12]. Therefore, an ideal OSM would be a stable compound that undergoes a rapid and robust reduction and reoxidation at the lowest possible temperature ($T \le 600$ °C).

Perovskite oxides with the general formula $ABO_{3-\delta}$ have received considerable interest due to their structural stability and flexibility upon cation substitution on the *A*- and/or *B*-site as well as lattice oxygen vacancies represented by a non-stoichiometry factor (δ)[15–18]. As one example, substituted $CaMnO_{3-\delta}$ perovskites have been explored as OSMs, but they require relatively high operating temperatures of 750-950 °C to

[a] National Energy Technology Laboratory, United States Department of Energy, 626 Cochran Mill Road, Pittsburgh, PA 15236, USA.
[b] NETL Support Contractor, 626 Cochran Mill Road, Pittsburgh, PA 15236, USA

Supplementary Information available: [The Supporting Information is available free of charge about the atomistic models of the pristine $BaFeO_{3-\delta}$, $Ba_{0.583}Sr_{0.417}FeO_{3-\delta}$, $BaFeO_{2.5+\delta}$ and $Ba_{1-x}Sr_xFeO_{2.5}$ OSMs and the phonon density of states of hexagonal and cubic OSMs. See DOI: 10.1039/x0xx00000x

achieve considerable oxygen storage capacity (OSC)[19,20]. $SrFeO_3$ is another perovskite OSM that has been heavily studied due to its ability to induce oxygen vacancies through oxygen release at T < 600 °C under inert atmospheres and rapid oxygen up take at temperatures 277-327 °C to re-oxidize its reduced phases in O_2 environment[21,22]. When operating isothermally at 400 °C, $SrFeO_{3-\delta}$ has an OSC of 0.84 wt.% when switching gas flow between air and N_2, which can be enhanced to 2.41 wt.% through compositional engineering with Ca^{2+} *A*-site substitution forming $Sr_{0.75}Ca_{0.25}FeO_{3-\delta}$[23,24]. This increase in oxygen storage activity occurs because the lattice oxygen binding energy decreases due to lattice strain caused by the incorporation of smaller Ca^{2+} cations[23,24]. Additionally, DFT modeling has suggested that Ca^{2+} substitution at x = 0.125–0.375 reduces the oxygen vacancy formation energy and lowers the oxygen migration barrier in $Sr_{1-x}Ca_xFeO_{3-\delta}$[25]. *B*-site substitution can further improve the oxygen storage activity of $Sr_{1-x}Ca_xFeO_{3-\delta}$ - based materials, typically through cobalt or nickel substitution. The use of cobalt drives fast reduction kinetics at lower operating temperatures (400-500°C)[14,26,27] whereas small amounts of nickel can dramatically improve reduction kinetics at similar temperatures[28]. With a high-throughput inverse ML workflow, several interesting new chemical looping material candidates of $SrFeO_3$ family namely $Sr_{1-x}A_xFe_{1-y}B_yO_3$ (e.g., *A* = Ca or K; *B* = Mg, Bi, Mn, Ni, Co, Cu, or Zn) are identified. These materials have shown promising properties, and some of them even outperform the $SrFeO_3$ material in terms of oxygen release kinetics[29].

Recently, $BaFeO_3$-based perovskites also have received attention as OSMs. While *B*-site substituted $BaCa_{0.2}Fe_{0.8}O_{3-\delta}$ is shown to operate well at 300-500 °C producing 2.41 $m^3_{O_2}kg^{-1}_{OSM}$ of oxygen at cycling experiments at 375 °C[30], *A*-site substitution with Sr^{2+} is also viable. Like Ca^{2+} substitution in the $Sr_{1-x}Ca_xFeO_{3-\delta}$ system, lattice strain can also be introduced when iso-valent and smaller Sr^{2+} partially substitutes Ba^{2+} in $Ba_{1-x}Sr_xFeO_{3-\delta}$ perovskites. At the temperature range 400-800 °C, Zhang et al.[31] has demonstrated the improvement in oxygen exchange capacity of $Sr_{0.5}Ba_{0.5}FeO_{3-\delta}$ over $SrFeO_{3-\delta}$, Bush et al.[32] found $Sr_{0.85}Ba_{0.15}FeO_{3-\delta}$ operate under temperature swing conditions, and Bektas et al.[33] identified $Sr_{0.75}Ba_{0.25}FeO_{3-\delta}$ as a promising OSM candidate for pressure swing between 0.01-0.2 atm O_2. Ongoing research efforts aim to identify and improve OSMs that can enhance efficiency of CLAS technology by requiring less energy input[30,34] and thermal strain than currently best performing materials that operate optimally at temperatures at or above 400 °C. For example, our recent work has indicated the importance of high surface area in OSMs to decrease the operating temperature and improve the reduction kinetics[35].

The formation thermodynamics of single or multiple oxygen vacancies and their diffusion kinetics using computational approaches under different scenarios can be used to identify promising candidates. In the $SrFe_{1-x}Co_xO_{3-\delta}$ oxygen carriers, the single oxygen vacancy formation energy was found to be related with concentration of substituent (Co)[36,37]. By using single oxygen vacancy formation energy in a machine learning (ML) approach, Ba-containing $Sr_{1-x}Ba_xFe_{1-y}Cu_yO_{3-\delta}$ perovskite was identified as a promising OSM[38]. This suggested composition agrees with experimental observation by Krzystowczyk et al.[39], which showed Ba and Cu substitution improves redox capacity. Despite the promising features of the Ba-containing perovskite oxides for OSMs, a limited number of first principles studies are available that quantify the redox thermodynamics of the $BaFeO_3$-based perovskites. Hoedl et al.[40] related trends in the reduction thermodynamics of $BaFeO_{3-\delta}$ and $Ba_{0.5}Sr_{0.5}FeO_{3-\delta}$ in the cubic phase with a higher Fermi level due to the presence of electrons left after the creation of oxygen vacancies. Rahmani et al.[41] suggested mechanical stability of the mixed structure in the cubic phase.

In this study, we quantify both the reduction and oxidation thermodynamic characteristics of $BaFeO_{3-\delta}$ as a parent structure and its iso-valent Sr^{2+} *A*-site substituted compounds at various oxygen concentrations in reported hexagonal and cubic phases. Since Sr^{2+} substitution alters the crystal structure of fully oxidized $Ba_{1-x}Sr_xFeO_3$ from hexagonal $BaFeO_3$[42,43] to cubic $SrFeO_3$[44], this system offers an opportunity to explore the effect of phase change on oxygen storage properties. Our study complements the recent experimental studies of pristine $BaFeO_3$[45,46] and substituted perovskites[30,33] from systematic incorporation of Sr^{2+} into $Ba_{1-x}Sr_xFeO_{3-\delta}$ (x = 0.0-0.417) and computationally investigating the effect of this change on the thermodynamics associated with multiple oxygen vacancy formation. Additionally, we explore the phase changes that occur upon Sr substitution on stoichiometric/non-stoichiometric perovskites to identify the minimum and maximum amount of Sr required to facilitate a pseudo-cubic structure at different oxygen concentrations. We then examine how these changes impact the oxygen storage properties of the material using DFT and experimental investigations including X-ray diffraction (XRD), oxygen-temperature-programmed desorption (O_2-TPD), and thermogravimetric analysis (TGA). Overall, we identify $Ba_{0.75}Sr_{0.25}FeO_{3-\delta}$ as the optimal $Ba_{1-x}Sr_xFeO_{3-\delta}$ composition for operating in an air/N_2 pressure swing system at low temperatures of 325 °C and 350 ^{0}C.

Computational and Experimental Details

Density Functional Theory (DFT) Calculations

Similar to previous computational studies on $Sr_xCa_{1-x}FeO_{3-\delta}$ OSMs[24,25,36–38,47,48], DFT[49,50] calculations were performed in this work using the Vienna *Ab-Initio* Simulation Package (VASP) code[51]. The valence electrons were represented by plane wave functions obtained with a kinetic energy cut-off at 850 eV. The interaction of the valence electrons (Ba: $5s^2\ 5p^6\ 6s^2$; Sr: $4s^2\ 4p^6\ 5s^2$; Fe: $3s^2\ 3p^6\ 4s^1\ 4d^7$; and O: $2s^22p^4$) with the ionic cores were treated using the projector augmented-wave (PAW)[52,53] potentials. The contribution of electron-electron exchange correlation interaction on the total energy was treated in the generalized gradient approximation (GGA) at PBEsol[54] scheme. To identify the energetically preferred atomistic models, the supercells were optimized by allowing atomic positions, cell shape, and volume to change using the conjugate gradient algorithm until the energy difference between successive

electronic iterations and the Hellmann-Feynman forces on each atom became 10^{-6} eV and 10^{-2} eV/Å, respectively. The Brillouin zone of the $BaFeO_3$ unit cell was integrated by taking the k-point mesh density of 8 x 8 x 8 generated according to the Monkhorst-Pack scheme[55]. To overcome the well-known limitation of the DFT method to properly treat the electronic self-interaction in localized Fe *d*-orbitals, the DFT+*U* method[56] with U_d = 5.0 eV was employed.

To test the effect of spin orientation on the energy of a compound, we compared the total energies of ferromagnetic (FM), *A*-type antiferromagnetic (*A*-AFM), *C*-AFM, and *G*-AFM spin ordered structures (Fig. S1) on example compounds. $BaFeO_3$, $Ba_{0.8}Sr_{0.2}FeO_3$ and $Ba_{0.583}Sr_{0.417}FeO_{3-\delta}$ are taken as representatives of a pristine compound, a compound with Sr substitution, and a compound with both Sr substitution and oxygen vacancies, respectively. The differences in total energy presented in Table S1 show the structure with Fe spins ordered in FM state has the lowest energy for all our example compounds. The result agrees with ref.[57] for $BaFeO_3$ and thus we assume the FM spin order of Fe atoms for all explored compounds in this study.

To find the minimum energy path and the activation energy barrier of an oxygen diffusion process to a vacancy site, the Climbing-Image Nudged Elastic Band (CI-NEB) method[58] implemented in the VASP package was used. We interpolated five images between the initial and final structures to generate a guess pathway.

To explore the possibility of thermally induced structural phase transitions, we compared the Helmholtz free energy *F*(T) of a compound at different phases. The *F*(T) was calculated by using

$$F(\mathrm{T}) = \int_0^\infty [\frac{\hbar\omega}{2} + \mathrm{k_B T} \ln (1 - \mathrm{e}^{-\frac{\hbar\omega}{\mathrm{k_B T}}})]\, \rho\,(\omega)\, \mathrm{d}\omega, \quad (1)$$

in which the phonon frequencies (ω) were calculated by using the finite difference method and supercell approach implemented in the phonopy package[59]. To calculate the force constants, atoms in a 2 x 2 x 3 supercell of bulk ABO_3 were displaced from their relaxed position with an amplitude of 0.015 Å. Phonon density of states $\rho\,(\omega)$ were calculated by sampling the Brillouin zone with 30 x 30 x 20 q-point mesh for cubic supercell with a smearing width of 0.05 THz. The phonon density of states was used to confirm the thermodynamic stability of atomistic models.

Experimental Procedures

$Ba_{1-x}Sr_xFeO_{3-\delta}$ (x = 0.0, 0.08, 0.17, 0.25, 0.33, 0.42, 0.5, and 1.0) samples were synthesized through a traditional bulk solid-state method established in our prior work[24,35]. Briefly, barium (II) carbonate ($BaCO_3$, Alfa, 98%), strontium (II) carbonate ($SrCO_3$, Aldrich, 99.8%), and iron (III) oxide (Fe_2O_3, Alfa, 99.9%) were added to an agate mortar in stoichiometric quantities matching the desired substitution level. These precursors were manually ground into a homogeneous mixture. This mixture was then pressed into a 13-mm pellet which was then loaded into an alumina combustion boat. This sample was then primed in air at 850 °C for 40 hours in a box furnace. Following this initial priming, the pellet was reground, repelletized, and then calcined at 1000 °C for 64 hours. The final compound was then stored as a ground powder in a scintillation vial.

Powder X-ray diffraction (pXRD) patterns were collected using a PANalytical X'Pert Pro XRD using Cu Kα radiation source (λ = 1.541 Å) in a Bragg-Brentano configuration. A 5-80° 2-theta range was used with a 0.006° step size.

Thermogravimetric analysis (TGA) of our OSMs was performed using a Mettler-Toledo TGA/DSC3+ using methods established in our prior work[24,35]. To begin, pretreatment was performed by heating at 10 °C/min to 800 °C in zero-grade (ZG) air (75 standard cubic centimeters per minute), then switching to ultra-high purity (UHP) N_2 (75 sccm) for 30 min at 800 °C and cooling to room temperature. This experiment was repeated to characterize the oxidation properties of our systems. Following these two experiments, cyclic testing was performed isothermally at 325 °C and 350 °C. Using 350 °C as an example, the system was heated to the desired operating temperature in ZG air in two steps: 1) 20 °C/min to 250 °C, and 2) 10 °C/min to 350 °C. Once the operating temperature was reached, gas flow was switched between UHP N_2 and ZG air every 60 min until four N_2/air cycles were completed.

The value of δ in our as-made systems was estimated by reducing the tested system at 800 °C for 30 minutes under UHP N_2 flow and allowing up take in ZG Air upon cooling. This cooling step was split between a 10 °C/min ramp rate from 800-350 °C, held at 350 °C for 10 minutes, and cooled further to 30 °C at 5 °C/min. This stepped up take method was developed to ensure maximum oxygen up take, while not requiring a slow 1.5 °C/min ramp rate as used in our synthesis.

O_2-TPD experiments were carried out in a Micromeritics Autochem 2950 HP analyzer equipped with a Pfeiffer Vacuum ThermoStar mass spectrometer. The gas flow rates, and temperature ramp rates were 50 sccm and 10 °C/min, respectively. Initially, approximately 250 milligrams (mg) of the sample were loaded in a U-shaped quartz cell packed with quartz wool and then pretreated in flowing ZG air at 800 °C for 1 hour. Following cooling to room temperature in air, the sample was heated to 1000 °C in UHP Ar while O_2 (*m/z* = 32) desorption was monitored by the mass spectrometer. The quantity of oxygen release observed in these experiments corroborates with our estimation of δ using TGA.

Results and Discussion

Structure of the $BaFeO_{3-\delta}$

$BaFeO_3$ is known to exist in hexagonal [45,60–63] and cubic structure [64,65] at normal and oxygen-rich synthesis conditions, respectively. Overall, three major structures exist for $BaFeO_3$. First, the 6*H* hexagonal polymorph that contains combination of corner- and face- sharing octahedra (Fig. 1a) can be formed at high temperatures and ambient pressure. This structure has FeO_6 octahedra repeat every six layers along the *c*-axis in a …*ABCC'B'A'*… sequence, with ' referring to a reversed octahedra orientation. Within the unit cell, our calculated magnetic moments of Fe (1) and Fe (2) type are found to be 3.592 μ_B

(reported value of 3.58 μ_B[66]) and 3.942 μ_B (reported value of 3.99 μ_B[66]), respectively.

Second, the 12*H* hexagonal polymorph is a 12 layered structure consisting of face-sharing Fe_3O_9 octahedral trimers and corner-sharing octahedra. This structure forms at high temperature and high-pressure oxidation conditions. Among the reported models of 12*H* polymorph at different space groups, our calculations found that it at the monoclinic *C*2/*m* space group (Fig. 1b) with initial geometrical parameters from Tan et al. [45] and Watanabe et al. [46] are within 0.5 meV with the energy of the rhombohedral *R*-3*m* space group structure from Tan *et al*. [45]. These structures are degenerate within the error bar of DFT calculations, and the former model is taken to represent the 12*H* structure in this work. The calculated magnetic moments of Fe(1), Fe(2), and Fe(3) are 3.868μ_B, 3.836μ_B, and 2.888μ_B agree qualitatively with respective measured values of 3.6 μ_B, 4.12 μ_B and 2.74 μ_B reported by Tan et al. [45].

Lastly, the 3*C* polymorph represents the traditional cubic perovskite structure with FeO_6 octahedra connected only via corner-sharing oxygen. The BaO_3 close-packed layers have …*ABCABC*.. stacking order along the <111> direction (Fig. 1c). This structure typically forms at low-temperature and at high oxygen environment. Only one type of Fe is found in the 3*C* structure which we calculated to have magnetic moment of 3.788 μ_B, slightly higher than the measured value of 3.5 μ_B[65].

To identify the atomistic models of $BaFeO_{3-\delta}$ structures, we compare the DFT computed energy of the optimized 6*H*, *12H,* and *3C* structures. Our calculations find the 12*H* structure is energetically preferred model of $BaFeO_3$ (Table I) over 6*H* and 3*C*, agreeing with the experimental measurement of the phase[45,67]. The energetic advantage for preference of hexagonal structure is realized by mitigating the strain induced when the larger Ba^{2+} ($R_{Ba^{2+}} = 1.61$ Å) occupies the cubo-octahedral cavity of FeO_6 formed by the Fe^{4+} cations of small ionic radius ($R_{Fe^{4+}} = 0.585$ Å) and oxygen anion ($R_{O^{2-}} = 1.61$ Å).

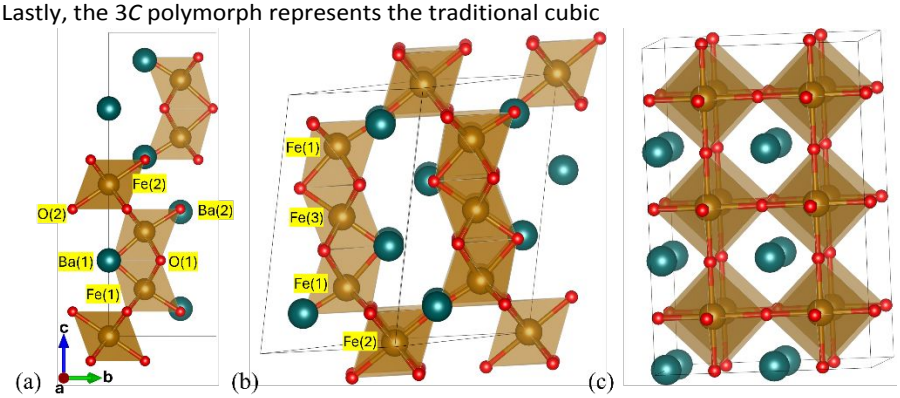

Fig. 1. The atomistic structures of $BaFeO_3$ in the (a) hexagonal 6*H* polymorph, (b) hexagonal 12*H* polymorph structure with the *C*2/*m* space group, and (c) Cubic structure at 2 x 2 x 3 supercell structure. The green, gold, and red spheres represent Ba, Fe, and O atoms, respectively. Structurally asymmetric Ba, Fe, and O atoms are labeled when necessary. In the 6*H* polymorph, the four Fe cations in face-shared octahedra are labeled Fe(1) while and other two at corner-shared octahedra are labeled Fe(2). The oxygen anions located on the layer between the Fe(1) cations are labeled O(1), while those situated between Fe(1) and Fe(2) are labeled O(2). Ba^{2+} cations adjacent to face-sharing and corner-sharing FeO_6 octahedra are labeled Ba(1) and Ba(2), respectively. In the 12*H* polymorph, three different type of Fe sites: Fe(1) and Fe(3) located respectively within the outer and inner octahedra of the Fe_3O_9 trimer and Fe(2) located in the corner-sharing octahedra are labeled.

Table I. The energy of $BaFeO_3$ polymorphs from that of the energetically preferred 12*H* model (E_{12H} =-33.526 eV/formula unit) and the geometric parameters. The reported values from experimental measurements and other computational studies with different values of effective *U* parameter (U_{eff}) are presented in parenthesis.

$BaFeO_3$	ΔE(meV per f.u.)	Geometrical Parameters (Å)
12*H*	0	*a* = 9.840 (9.859[45])
		b = 5.681 (5.699[45])
		c = 9.849 (9.898[45])
		d(Fe(1)-Fe(3)) = 2.065 (2.05[46])
		d(Fe(2)-Fe(3)) = 2.581 (2.615[46])
6*H*	21.61	*a* = 5.653 (5.674[60], 5.672[68], 5.6743[69], 5.673[62], 5.66[46], Computed: 5.69[66] at U_{eff} = 4 eV)
		b = 5.653
		c = 13.820 (13.74[60], 13.90[68], 13.929[69], 13.921[62], 13.87[46] Computed: 13.815[66] at U_{eff} = 4 eV)
		d(Fe(1)-Fe(2)) = 2.142 (2.15[46])
		d(Fe(1)-Fe(1)) = 2.626 (2.65[46])
3*C*	114.69 (70 [70])	*a* = *b* = *c* = 3.958 (3.971[65], 3.97[71](Computed: 4.015[70], 3.963[72] at U_{eff} = 3 eV, 3.995[73] at U_{eff} = 4 eV)

ARTICLE

Oxygen Vacancy Formation in $BaFeO_{3-\delta}$

$BaFeO_{3-\delta}$ OSMs have been reported for various values of δ from 0.0 to 0.5. To computationally identify the energetically preferred models of $BaFeO_{3-\delta}$ and to calculate their oxygen vacancy formation energies, we iteratively introduced oxygen vacancies into the previously discussed 12*H*, 6*H*, and 3*C* models of the $BaFeO_3$ structure at 1 x 3 x 1, $2\sqrt{2}$ x $2\sqrt{2}$ x 3, and 2 x 2 x 3 supercell models, respectively. The energy of preferred phase along with lattice parameters presented in Table II shows the preference of hexagonal structures versus the 3*C* structures for any amount of oxygen vacancies introduced in $BaFeO_{3-\delta}$. The 12*H* polymorph is favored when minimal oxygen vacancies are present, specifically $BaFeO_3$ and $BaFeO_{2.958}$, whereas the 6*H* phase is favored when $0.0417 < \delta \leq 0.458$. This result also corroborates with experimental observations of the 12*H* phase in $BaFeO_{2.95}$[60] and $BaFeO_{2.93}$[74] while the 6*H* phase exists between $BaFeO_{2.63}$ and $BaFeO_{2.95}$[60,68,75]. It is important to note that there are some inconsistencies among experimental measurements regarding the crystalline phases within this composition range. For example, Mori et al. identified the existence of cubic, tetragonal, and monoclinic phases for $BaFeO_{2.5}$ to $BaFeO_{2.92}$[68], Takeda et al. measured 12*H* for $BaFeO_{2.83}$[67] and Parras et al. measured mixed 6*H* and 10*H* phases for high oxygen containing $BaFeO_{2.95}$[61]. The inconsistencies are likely due to differences in methodology, instrument capability, and interpretation used to determine both δ and the crystal structure.

The atomistic models of some of $BaFeO_{3-\delta}$ systems from our calculations are presented in Fig. S2. The lattice parameters of optimized $BaFeO_{3-\delta}$ OSMs obtained from our calculations along with available experimental values presented in Table II show excellent agreement. Additionally, in Table II, the lattice parameters of the supercells increase upon creation of successive oxygen vacancies. Intuitively, the creation of oxygen vacancies removes attractive forces between the metal cations and oxygen anions and/or increase the repulsive forces between the cations resulting in the volume increase. At an electronic level, vacancy introduction generates an empty defect in the density of states close to the Fermi level because two electrons are left behind when the neutral vacancy forms. This is identified as a mechanism for the overall volume expansion[76,77].

Table II. The DFT computed energy per formula unit (*E*) and lattice parameters of the $BaFeO_{3-\delta}$ perovskites on energetically favored structures. The corresponding values from experimental measurements are presented in parenthesis.

δ	*E* (eV)	*a* (Å)	*b* (Å)	*c* (Å)
0 (12*H*)	-33.526	9.840 (9.859[45])	5.681 (5.699[45])	9.849 (9.898[45])
0.0417 (12*H*)	-33.280	9.845	5.688	9.876
0.0417 (6*H*)	-33.276	5.659 (5.674[60], 5.671[61], 5.664[63])	5.657	13.854 (13.74[60], 13.873[61], 13.878[63])
0.0834 (6*H*)	-33.047	5.663 (5.692[74] 5.672[68])	5.665	13.886 (13.991[74] 13.90[68])
0.125 (6*H*)	-32.812	5.669 (5.684[63])	5.673	13.917 (13.957[63])
0.167 (6*H*)	-32.576	5.671 (5.69[60])	5.672	13.953 (13.89[60])
0.208 (6*H*)	-32.324	5.677 (5.683[78])	5.678	13.985 (14.062[78])
0.25 (6*H*)	-32.073	5.686	5.683	14.02
0.292	-31.814	5.696	5.688	14.065
0.334 (6*H*)	-31.542	5.707 (5.683[79])	5.703	14.101 (13.916[79])
0.375 (6*H*)	-31.258	5.724 (5.74[60])	5.714	14.121 (13.86[60])
0.417 (6*H*)	-30.979	5.743	5.732	14.142
0.458 (6*H*)	-30.689	5.758	5.734	14.152
0.5 (Mono-clinic)	-30.301	5.796 (5.83[60] 5.911[79])	15.599 (16.38[60], 16.45[79])	5.875 (5.54[60], 5.518[79])

To understand the complexities required to adequately describe the oxygen storage process, we calculated the oxygen vacancy formation energy ($E_{O\ vac}$). The oxygen vacancy formation requires breaking a metal-oxygen bond and is the most energy intensive step in a complex oxygen release

process. Since the strength of a metal-oxygen bond on a surface structure of a perovskite and other oxides correlates with that in bulk[80], we calculated the $E_{O\ vac}$ in the bulk model to quantify a system's tendency to release oxygen by using

$$E_{O\ vac} = E_{defect} + \frac{n}{2} E_{O2} - E_{supercell}, \quad (2)$$

where $E_{supercell}$, E_{defect}, and E_{O2} are the energy of the supercell (Table I), supercell with *n*-number of oxygen vacancies (Table II), and an O_2 molecule (E_{O2} = -10.256 eV from spin-polarized calculation[18]), respectively. A positive and negative $E_{O\ vac}$ represents an endothermic and exothermic process, respectively.

In the 12*H* model of $BaFeO_3$, our calculations found the removal of the oxygen at the face-shared octahedra between Fe(1) and Fe(3) in Fig. 1b is the energetically most preferred with $E_{O\ vac}$ = 0.773 eV. This reduces our model to $BaFeO_{2.958}$. For comparison purpose, the $E_{O\ vac}$ for the energetically disfavored 6*H* and 3*C* polymorphs of $BaFeO_3$ are 0.344 eV and 0.12 eV, respectively. TGA measurements of the reduction in these three polymorphs by Watanabe corroborate our findings, with the 12*H* being the most difficult to reduce (460 °C) and 3*C* the easiest (130 °C)[46].

When introducing additional oxygen vacancies past δ > 0.0417, we only considered 6*H*-$BaFeO_{3-\delta}$ structures because it is the energetically favorable phase. The oxygen in the face-sharing O(1) sites are thermodynamically preferred for vacancy formation when 0.0417 ≤ δ ≤ 0.334. This agrees with the previous work by Watanabe et al.[46]. For additional vacancies formation for 0.334 < δ ≤ 0.5, the oxygens at O(2) sites are favored. The atomistic models of the $BaFeO_{3-\delta}$ OSMs depicting the oxygen vacancy formation sites are presented in Fig. S2. The $E_{O\ vac}$ per oxygen vacancy increases monotonically as additional vacancies are introduced. For δ = *n* x 0.0417 with the number of oxygen vacancies (*n*) = 1, 2, 3, ...,12, the $E_{O\ vac}$ per oxygen vacancy are 0.356, 0.367, 0.419, 0.45, 0.545, 0.605, 0.675, 0.767, 0.871, 0.939, 1.021, and 1.152, respectively.

Effect of Sr-Substitution on Oxygen Desorption in $Ba_{1-x}Sr_xFeO_{3-\delta}$

While $BaFeO_{3-\delta}$ has been well-studied experimentally, expanding our work to substitute Sr^{2+} at Ba^{2+}-site has been less explored. The Goldschmidt tolerance factor (*t*)[81] can be predictive in determining the perovskite for given *A*-, *B*-, and O-site compositions which is defined as

$$t = \frac{R_A + R_O}{\sqrt{2}(R_B + R_O)}, \quad (3)$$

where R_A,R_B, and R_O are the ionic radii of *A*, *B*, and O of ABO_3 perovskite, with 1 corresponding to an ideal cubic perovskite phase. For $BaFeO_3$, *t* = 1.08 which supports hexagonal structure formation. However, the partial Sr^{2+} substitution for Ba^{2+} on the *A*-site lowers this value closer to 1 due to the smaller ionic radius of Sr^{2+}. To explore this change, we examined the crystal structure variation of $Ba_{1-x}Sr_xFeO_{3-\delta}$ using pXRD. The patterns of the Sr^{2+}-substituted $Ba_{1-x}Sr_xFeO_{3-\delta}$ (0 ≤ x ≤ 1) presented in Fig. 2 show that the preference toward the hexagonal phase of $BaFeO_{3-\delta}$ does not continue at x ≥ 0.083. At x = 0.083, we observe a mixture of the hexagonal phase with a separate pseudo-cubic phase (cubic, tetragonal, or orthorhombic). As the Sr^{2+} content increases (x ≥ 0.167), the hexagonal phase is no longer observed and the major [011] reflection of the pseudo-cubic structure shifts towards higher 2θ values due to unit cell contraction.

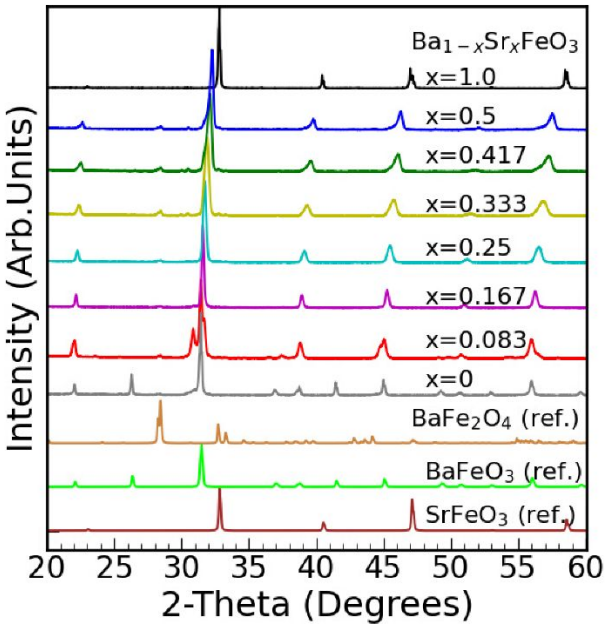

Fig. 2. XRD patterns of the $Ba_{1-x}Sr_xFeO_{3-\delta}$ (0 ≤ x ≤ 1) samples.

With experimental evidence of the hexagonal-to-cubic transition as predicted by the *t* (equation (3)), we used DFT to investigate the energetic preference of $Ba_{1-x}Sr_xFeO_{3-\delta}$ between the hexagonal or cubic phase as x and δ are changed. We used a matrix of x = 0.083, 0.167, 0.25, 0.333, and 0.417 and δ = 0.0, 0.083, 0.167, 0.25, and 0.333 to determine the energetic structural preference at each composition.

When no oxygen vacancies are present in the structure (δ = 0), hexagonal structures are preferred at Sr^{2+} substitution below x = 0.417 and the 3*C* structure at x ≥ 0.417 (Fig. 3a). The atomistic models of the δ = 0 compounds in Fig. 3 depicts that the Sr^{2+} cations substitute the Ba (1), Ba (2), Ba (2), Ba (1) type sites at the nearest neighbor separation in preferred 6*H* based models at x = 0.083, 0.167, 0.25, and 0.333, respectively, while a layered arrangement of Sr^{2+} cations forms in preferred 3*C* based models at x = 0.417 and 0.5. We further corroborate the phase transition calculated at the x = 0.417 threshold using vibrational analysis. The phonon density of states of the hexagonal $Ba_{0.583}Sr_{0.417}FeO_3$, hexagonal $Ba_{0.667}Sr_{0.333}FeO_3$, and cubic $Ba_{0.583}Sr_{0.417}FeO_3$ compounds in Fig. S3 shows that the former is unstable as evidenced by a vibrational mode with an imaginary frequency, while he later two are thermodynamically stable. These DFT results of demonstrating a preference for the cubic phase as Sr^{2+} substitution increases agree qualitatively with our experimental findings shown in Fig. 2. Our calculated phase transition at x = 0.417 closely agrees with the experimental measurement of the hexagonal phase up to *x* = 0.35 when $Ba_{1-x}Sr_xFeO_{3-\delta}$ is synthesized under high O_2 pressures[43]. However, the hexagonal-to-cubic threshold is much lower in our

experimental findings from materials synthesized in air at ambient pressures. Given the reliance of the structural preference of $BaFeO_{3-\delta}$ on oxygen pressure, this mismatch is unsurprising. Under a third set of synthesis conditions, the hexagonal-to-cubic transition has also been reported at x = 0.2[62].

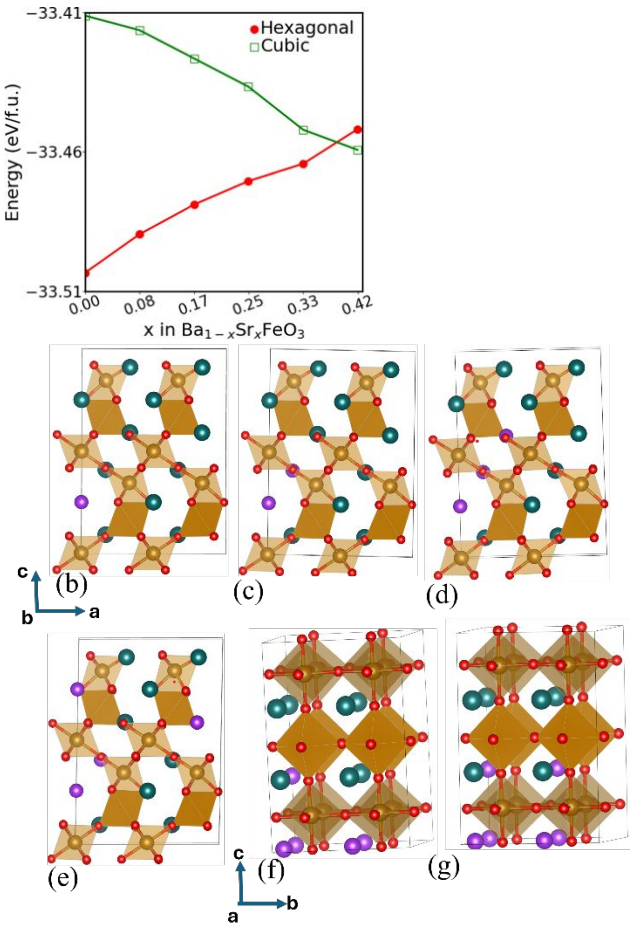

Fig. 3. (a) Variation of energy per formula unit of the $Ba_{1-x}Sr_xFeO_3$ formed on hexagonal and cubic based phases with concentration of substituted Sr cations. (b-f) The atomistic models of the energetically favored $Ba_{1-x}Sr_xFeO_3$ at x = 0.083, 0.167, 0.25, 0.333, 0.417, and 0.5. The green, gold, red, and purple spheres represent Ba, Fe, O, and Sr atoms, respectively.

To rationalize the energetic switching of the phase of $Ba_{1-x}Sr_xFeO_{3-\delta}$ OSMs as function of Sr^{2+} substitution concentration (x) at fundamental level, we present the electronic density of states (DOS) of $Ba_{1-x}Sr_xFeO_3$ at x = 0.083, 0.25, and 0.417 in the hexagonal and cubic based phases in Fig. 4. In Fig. 4a, the electronic occupancy at spin up states near the Fermi level (E_F) decreases with increasing Sr^{2+} substitution in the hexagonal phase. This decrease is less drastic in the cubic phase. The difference between the two phases is most prominent in $Ba_{0.583}Sr_{0.417}FeO_3$ correlating well with the phase switching expected and observed between the hexagonal and cubic phases. In Fig. 4b, the hybridization of the Fe-*d* orbitals with O(1) *p*-orbitals of 6*H* phase or oxygen of cubic $BaFeO_3$ is higher than that with O (2) type at hexagonal $BaFeO_3$. The lower $E_{O\ vac}$ from the former two sites over the latter implies that the Fe *d*-hybridization with O-*p* orbitals inversely related with the $E_{O\ vac}$.

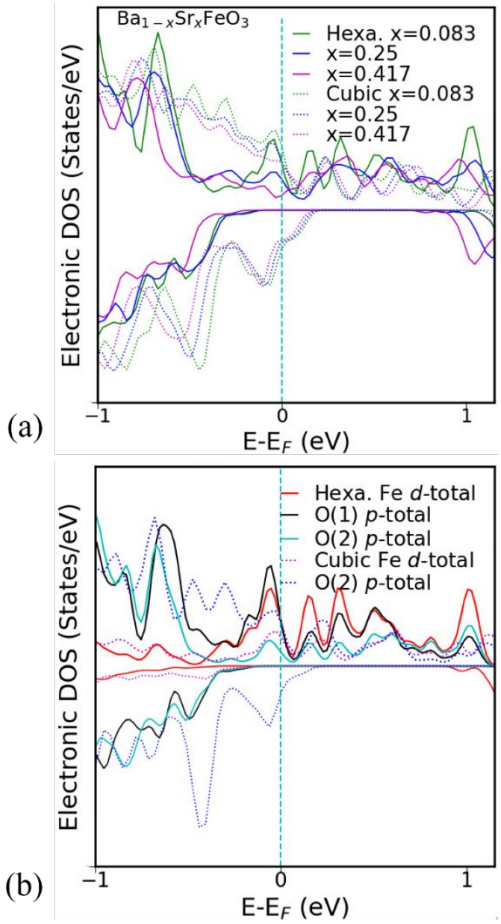

Fig.4. The electronic density of states (DOS) of (a) $Ba_{1-x}Sr_xFeO_3$ (x = 0.083, 0.25, and 0.417) OSMs at cubic and hexagonal phases near the Fermi level (E_F). (b) The DOS contribution from the Fe-*d* and O-*p* orbitals of cubic $BaFeO_3$ and from O (1) and O (2) type of oxygens in hexagonal $BaFeO_3$ OSMs (defined in Fig. 1a) near the E_F. The DOS of spin down orbitals are plotted in negative y-axis for visual convenience.

To explore the influence of magnetic state on the electronic structure of the target materials, we present the variation of the projected density of *d*-orbitals of an Fe cation on up and down spin components of the target cubic $Ba_{0.583}Sr_{0.417}FeO_3$ OSM. Irrespective of the FM, *A*-AFM, *C*-AFM, and *G*-AFM magnetic states, the Fes coordinated with Sr and Ba layers (see Fig. 3f) have the lowest magnetic moment while those coordinating with only Ba layers have relatively higher magnetic moments. The tendency of having high or low magnetic moments based on local neighborhood than that depending on the spin orientation implies the strong effect of the local neighborhood on the occupancy of *d*-orbitals. The Fe with high magnetic moment has values 3.776 μ_B, 3.905 μ_B, 3.844 μ_B, and 3.901 μ_B on the FM, *A*-AFM, *C*-AFM, and *G*-AFM states, respectively

which do not change significant magnetic state dependence. The Fe with the low magnetic moment has values 3.678 μ_B on the energetically favored FM while 3.541 μ_B, 3.659 μ_B, and 3.386 μ_B on the *A*-AFM, *C*-AFM, and *G*-AFM magnetic states, respectively. In Fig.5a and 5b, we show the PDOS of Fe with high and low moments, respectively. Irrespective of magnetic state, there is similar asymmetry in occupancy of up and down spin states, significant dispersion of the Fe 3*d*-orbitals over the long energy range leading to their hybridization with O 2*p* orbitals implying metallic nature.

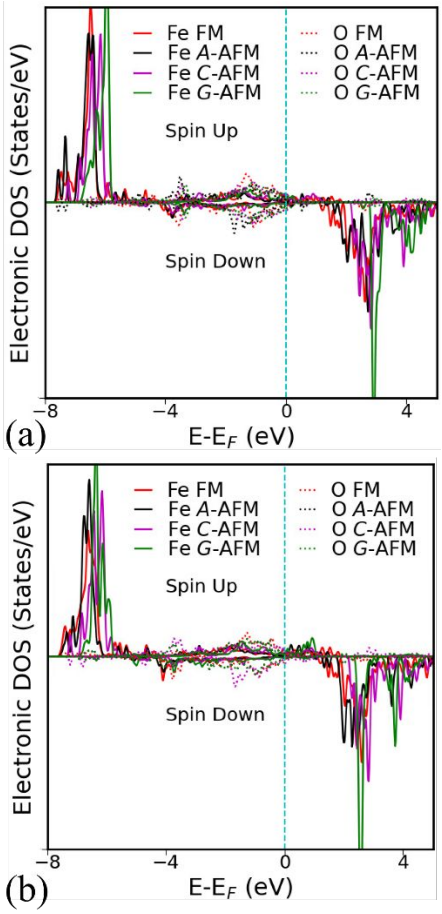

Fig. 5. The variation of the electronic density of states of Fe 3*d*-orbitals in $Ba_{0.583}Sr_{0.417}FeO_3$ with ferromagnetic (FM), *A*-type antiferromagnetic (*A*-AFM), *C*-AFM, and *G*-AFM magnetic ordering of Fe in lattice. The plot (a) and (b) correspond to Fe on the layer between Ba and Sr layers and between Ba layers (see model in Fig. 3f), respectively. The PDOS of oxygen 2*p*-orbitals are presented to depict the hybridization.

Since the oxygen vacancy concentration is relevant for CLAS, we introduce such vacancies into our $Ba_{1-x}Sr_xFeO_3$ models. Like in $Ba_{1-x}Sr_xFeO_3$, the energetic preference of phase of the non-stoichiometric $Ba_{1-x}Sr_xFeO_{3-\delta}$ changes after a threshold Sr concentration. The computed energies of $Ba_{1-x}Sr_xFeO_{3-\delta}$ systems with δ = 0.25 presented in Fig. 6 depict that the required Sr^{2+} threshold for phase switching is at x = 0.25. The results for systems with δ = 0.083, 0.167, and 0.333 presented in Fig. S4 depict the energetic preference from 6*H* to 3*C* at x = 0.25, below 0.25, and 0.25, respectively. Thus, Sr^{2+} substitution can switch the energetic preference from hexagonal to cubic phase and its required threshold decreases with the presence of oxygen vacancies in the OSM. The lattice parameters of these $Ba_{1-x}Sr_xFeO_{3-\delta}$ models in Table S2 match closely with reported measured values for some overlapping compositions in the literature[62].

Our experimental synthesis of the $Ba_{1-x}Sr_xFeO_{3-\delta}$ compounds in air by varying Sr^{2+} content from x = 0.083 to x = 0.5 observe compounds in a narrow oxygen non-stoichiometry (3-δ) distribution from 2.75 to 2.81 with higher Sr^{2+} contents leading to larger 3-δ values (Fig. S5). These materials are predominantly cubic, agreeing qualitatively with our computed results. The $BaFeO_{3-\delta}$ falls outside this narrow distribution with $BaFeO_{2.69}$ observed (Fig. S5). The hexagonal structure observed experimentally agrees with our computational findings, even at a high δ value (0.31).

To visualize the successive oxygen vacancy formation sites in the cubic phase, the atomistic models of $Ba_{0.583}Sr_{0.417}FeO_{3-\delta}$ with δ = 0.083, 0.167, 0.25, 0.333, and 0.5 are presented in Fig. S6. We find the oxygen on apical sites with Sr on local neighborhood are preferred to create oxygen vacancies being independent of the Sr^{2+} concentration in the cubic phase.

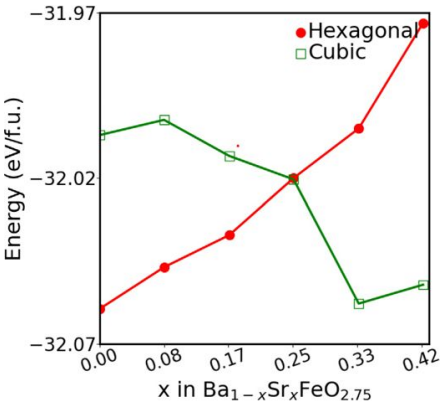

Fig. 6. Variation of total energy per formula unit of the $Ba_{1-x}Sr_xFeO_{2.75}$ formed on hexagonal and cubic based phases with concentration of substituted Sr^{2+} cations at x = 0.083, 0.167, 0.25, 0.333, and 0.417.

To investigate an inherent advantage of this phase transition on oxygen release tendency, we calculated and compared $E_{O\ vac}$ corresponding to δ = 0.083, 0.167, 0.25, and 0.333 on $Ba_{1-x}Sr_xFeO_{3-\delta}$ (x = 0, 0.25, and 0.417) with those of two well-studied OSMs namely $SrFeO_{3-\delta}$ and $Sr_{0.75}Ca_{0.25}FeO_{3-\delta}$. The comparison presented in Fig. 7a shows that the $E_{O\ vac}$ in cubic $Ba_{0.583}Sr_{0.417}FeO_{3-\delta}$ are the lowest for all values of δ among our explored materials. In addition, we compared the $E_{O\ vac}$ of hexagonal and cubic $Ba_{1-x}Sr_xFeO_{3-\delta}$ OSMs at δ = 0.0, 0.083, 0.167, 0.25, and 0.333 in Fig. 7b that shows consistently smaller $E_{O\ vac}$ in cubic OSMs than corresponding values in hexagonal OSMs, with the largest difference in creating the initial set of

oxygen vacancies. Thus, the formation of a cubic $Ba_{1-x}Sr_xFeO_{3-\delta}$ OSMs by incorporating sufficient Sr^{2+} on Ba^{2+} sites is vital for oxygen release performance. Furthermore, the difference in free energies of the hexagonal and cubic phase of $Ba_{0.583}Sr_{0.417}FeO_{3-\delta}$ shown in Fig. 7c remains positive with variation in temperature, suggesting the cubic phase obtained has tendency to be stable even at elevated temperatures. The opposite, both positive and negative free energy differences between the two phases, is obtained for $BaFeO_3$ implying a temperature-dependent transition from hexagonal to cubic. The transition temperature obtained at approximately 700 °C agrees qualitatively with measured results by Mori et al. [68].

To explore the effect of the hexagonal-to-cubic phase change on the oxygen mobility, we calculated the activation energy barrier (E_a) of an oxygen diffusion from equatorial lattice site to a nearby vacancy on apical site (the sites are labeled in Fig. S7). The E_as are found to be 0.957 eV and 0.915 eV in $BaFeO_{2.958}$ and $Ba_{0.583}Sr_{0.417}FeO_{2.958}$, respectively (Fig. 8) implying small effect of Sr^{2+} substitution. These values are much larger than the E_a of 0.531 eV in $Sr_{0.75}Ca_{0.25}FeO_{2.958}$. Since Fe-O bond breakage and formation is naively related to the oxygen diffusion, we quantify the distance of the diffusing oxygen to the nearby Fes to intuitively rationalize the variation in E_a. The Fe-O distances to three different Fes (see Fig. S7 for labeling of sites of interest) on $Ba_{0.583}Sr_{0.417}FeO_{2.958}$ and $Sr_{0.75}Ca_{0.25}FeO_{2.958}$ presented in Table S3 shows that the *d*(Fe1-O) is the lowest at the transition state (TS) at reaction coordinate 3 (see energy profile in Fig. 8) in both OSMs. From similar calculations in $BaFeO_{2.958}$, we determine *d*(Fe1-O), *d*(Fe2-O), *d*(Fe3-O) to be 1.723 Å, 3.237 Å, and 3.233 Å, respectively. As a trend, the relatively long distance of diffusing oxygen from the initially close Fe1 and short distance to Fe2 and Fe3 at TS in $Sr_{0.75}Ca_{0.25}FeO_{2.958}$ than in $Ba_{0.583}Sr_{0.417}FeO_{2.958}$ and $BaFeO_{2.958}$ might be correlated to the relatively small oxygen diffusion barrier in the $Sr_{0.75}Ca_{0.25}FeO_{2.958}$ system than others explored in this study. This result agrees with the reported trend in the diffusion of adatom on metallic surface[82].

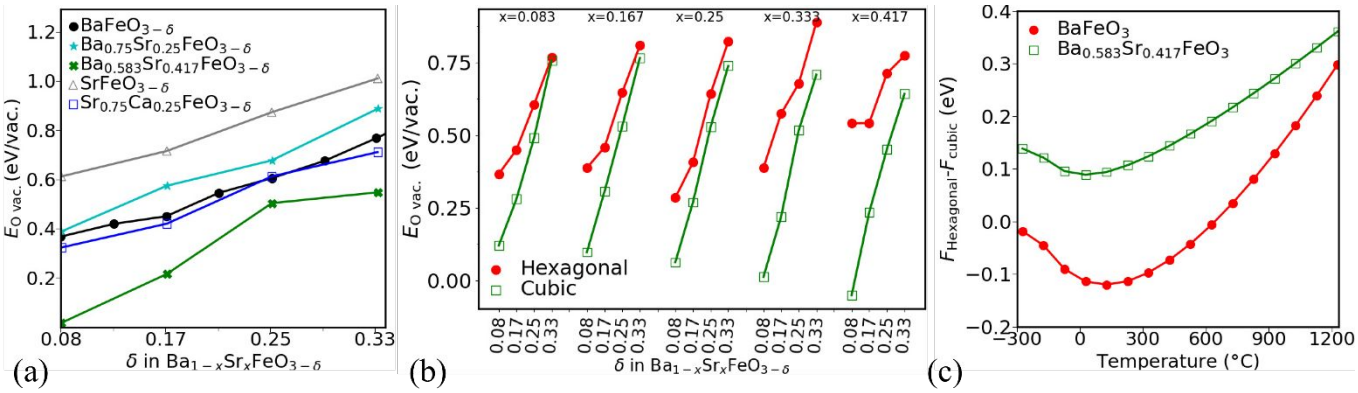

Fig. 7. Energetic advantage of Sr^{2+}-substitution induced phase change from hexagonal to cubic phase in $Ba_{1-x}Sr_xFeO_{3-\delta}$: (a) The comparison of oxygen vacancies formation energies ($E_{O\ vac}$) on $Ba_{1-x}Sr_xFeO_{3-\delta}$ (x = 0.0, 0.25, and 0.417) with those of the $Sr_{1-x}Ca_xFeO_{3-\delta}$ (x = 0.0, 0.25). (b) The $E_{O\ vac}$ on $Ba_{1-x}Sr_xFeO_{3-\delta}$ OSMs based on cubic and hexagonal phases. The concentration of Sr^{2+} cations on Ba^{2+} sites (x) are labeled at the top. For each x, oxygen vacancies at concentration δ = 0.083, 0.167, 0.25, and 0.333 are considered. (c) The variation of computed free energy difference of $BaFeO_3$ and $Ba_{0.583}Sr_{0.417}FeO_3$ in hexagonal and cubic phase with temperature.

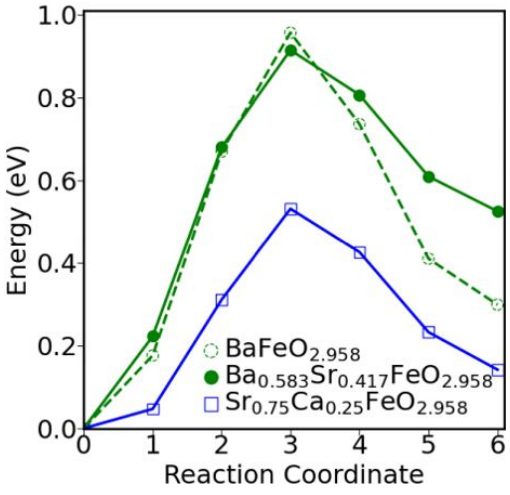

Fig. 8. The energy profile of an oxygen diffusion process from equatorial site to a vacancy on apical site of $BaFeO_{2.958}$, $Ba_{0.583}Sr_{0.417}FeO_{2.958}$, and $Sr_{0.75}Ca_{0.25}FeO_{2.958}$.

Given our findings that the cubic $Ba_{1-x}Sr_xFeO_{3-\delta}$ materials have smaller $E_{O\ vac}$ than their hexagonal counterparts, we experimentally investigated and compared O_2 desorption properties of eight of the $Ba_{1-x}Sr_xFeO_{3-\delta}$ (x = 0.0-1.0) compositions using O_2-TPD. The results presented in Fig. 9 shows onset temperature for O_2 desorption ranges from 205 °C to 227 °C, which is lower than that of $Sr_{0.75}Ca_{0.25}FeO_{3-\delta}$ (approx. 273 °C)[24,35]. This result aligns with our computed result of the lowest $E_{O\ vac}$ in $Ba_{0.583}Sr_{0.417}FeO_{3-\delta}$ (Fig. 7a). In Fig. 9, while the Ba/Sr containing materials generally have one major oxygen desorption step, $SrFeO_{3-\delta}$ (x = 1.0) and $BaFeO_{3-\delta}$ (x = 0) are outliers. Despite having the lowest onset temperature of ~200 °C, the $SrFeO_{3-\delta}$ requires much higher desorption temperatures

beyond its initial release due to its strong retention of oxygen. Interestingly, the O_2-TPD profile of $BaFeO_{3-\delta}$ similarly exhibits multiple unique desorption features not found in any of our other OSMs: an initial peak near 300 °C, an elongated release from 400-700 °C, and a final peak at ~800 °C. These features may align with the structural transition of the $BaFeO_{3-\delta}$ between 12*H*, 6*H*, and brownmillerite phases. Furthermore, there is a pronounced change in the desorption intensity at approximately 400 °C. The addition of a minimal amount of Sr^{2+} (x = 0.083) drastically alters the desorption profile of $BaFeO_{3-\delta}$. The highest intensity of O_2 desorption is achieved at x = 0.167, which is also the material with the lowest Sr^{2+} concentration that forms in a predominantly cubic or pseudo-cubic phase based on XRD patterns presented in Fig. 2.

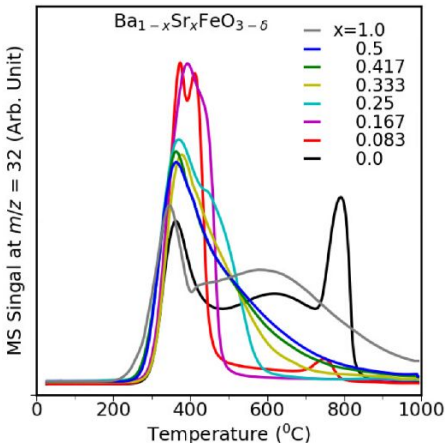

Fig. 9. The variation of oxygen desorption intensity of $Ba_{1-x}Sr_xFeO_{3-\delta}$ OSMs (x = 0.0, 0.08, 0.167, 0.25, 0.33, 0.41, 0.5, and 1.0) with temperature measured using O_2-temperature programmed desorption technique.

Oxygen Up take in $Ba_{1-x}Sr_xFeO_{2.5+\delta}$

For a competitive OSM, oxygen release must be reversible. For this reason, we quantified the oxygen up take (oxidation or absorption) features of the $Ba_{1-x}Sr_xFeO_{3-\delta}$ by using the $Ba_{1-x}Sr_xFeO_{2.5}$ brownmillerite phase as the reduced structure of both $BaFeO_3$ and the Sr^{2+}-substituted OSMs. Using a brownmillerite structure as the reduced phase follows the measured range of δ in $Ba_{1-x}Sr_xFeO_{3-\delta}$[75,83,84] and the energetic preference of the brownmillerite than the monoclinic phase of $BaFeO_{2.5}$[83] by 0.247 eV/f.u. in our calculations. Brownmillerite is an oxygen vacancy ordered three-dimensional structure that contains alternate stacking of the FeO_6 octahedra and FeO_4 tetrahedra with oxygen vacancies aligned along the [110] direction. The atomistic models of brownmillerite $BaFeO_{2.5}$ and its partially oxygenated forms from our calculations in Fig. S8 depict that the successively absorbed oxygen anions at the vacancies prefer to occupy distant sites initially and then the neighboring sites. The oxygen up take energy ($\Delta E_{\mathrm{Oxidation}}$) of an $ABO_{2.5+\delta}$ perovskite is calculated by using

$$\Delta E_{\mathrm{Oxidation}} = E_{ABO_{2.5+\delta}} - E_{ABO_{2.5}} - \delta \times \frac{E_{O_2}}{2}, \quad (4)$$

where $E_{ABO_{2.5}}$, $E_{ABO_{2.5+\delta}}$, and E_{O_2} are the energies of an $ABO_{2.5}$ supercell, an $ABO_{2.5+\delta}$ supercell with oxygen up take at concentration δ, and an O_2 molecule, respectively. We used an extended $2\sqrt{2}$ x 4 x $2\sqrt{2}$ supercell model to form the atomistic models of $BaFeO_{2.5+\delta}$ and $Ba_{1-x}Sr_xFeO_{2.5+\delta}$ to compute $\Delta E_{\mathrm{Oxidation}}$ so that interactions of incorporated oxygens with their periodic image will be avoided.

In Fig. 10a, the negative values of $\Delta E_{\mathrm{Oxidation}}$ calculated for the $Ba_{1-x}Sr_xFeO_{2.5+\delta}$ OSMs irrespective of the oxygen non-stoichiometry (δ) and Sr^{2+} substitution concentration (x) suggests the spontaneity of oxygen up take process. This preference is slightly weaker as Sr^{2+} concentration is increased. The atomistic models of $Ba_{1-x}Sr_xFeO_{2.5}$ OSMs at x = 0.125, 0.25 and 0.375 in Fig. S9 show that the successively substituted Sr^{2+} cations prefer to occupy the nearest neighbouring sites along [010] direction in a layer-by-layer manner so that the Sr layers are sandwiched between the Ba layers. The calculated lattice parameters of $BaFeO_{2.5+\delta}$, $Ba_{0.75}Sr_{0.25}FeO_{2.5+\delta}$, and $Ba_{0.5}Sr_{0.5}FeO_{2.5+\delta}$ OSMs at δ = 0.0, 0.125, 0.25, 0.375, and 0.5 are presented in Table S4 depicts that the orthorhombic brownmillerite phase of the OSMs gradually transforms into cubic phase in stoichiometric $Ba_{1-x}Sr_xFeO_3$. The volume of $Ba_{1-x}Sr_xFeO_{2.5+\delta}$ OSMs decrease consistently with increase in concentration of absorbed oxygen anions. This volume decrease upon oxygen absorption has a stronger effect than results from the substitution of Ba^{2+} with Sr^{2+}. For example, the volume of the $BaFeO_{2.5}$ decreases by 5.63 % and 1.86 % for oxygen up take at concentration δ = 0.5 and with Sr substitution at x = 0.5, respectively.

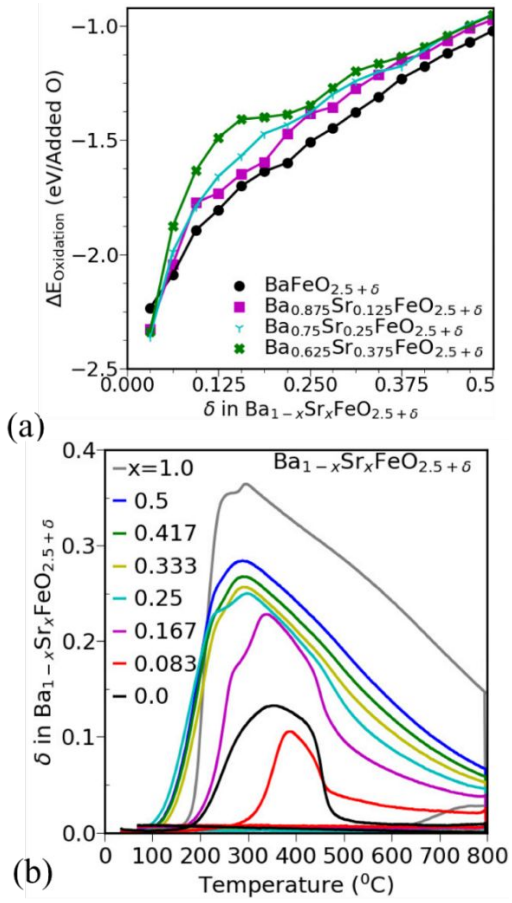

Fig. 10. (a) The calculated oxygen up take energy (per added oxygen) of $Ba_{1-x}Sr_xFeO_{2.5+\delta}$ OSMs (x = 0.0, 0.125, 0.25, and 0.375) as a function of the added oxygen concentration (δ). (b) TGA measured reoxidation of the $Ba_{1-x}Sr_xFeO_{2.5}$ OSMs at different temperature and Sr substitution concentration.

To corroborate these calculations, we performed TGA measurements of oxygen up take in $Ba_{1-x}Sr_xFeO_{2.5}$. Oxygen absorption was tracked by heating pre-reduced samples to 800 °C in air (21% O_2). The oxygen concentration (δ) is estimated from the mass change by assuming $Ba_{1-x}Sr_xFeO_{2.5}$ as a starting composition. The results in Fig. 10b depict that the OSMs with x ≤ 0.17 display an onset oxygen adsorption at/or above 150 °C while OSMs with x ≥ 0.25 begin up take at much lower temperatures (~ 100 °C). In Fig. 10a, increasing the Sr^{2+} content decreases $\Delta E_{Oxidation}$ for initial oxygen up take at δ = 0.031. The decrease $\Delta E_{Oxidation}$ is found to align with the decrease on the onset up take temperature. The maximum oxygen content in these materials increases systematically with Sr^{2+} content: δ = 0.1 for $BaFeO_{2.5+\delta}$, 0.28 for $Ba_{0.5}Sr_{0.5}FeO_{2.5+\delta}$, and 0.35 for $SrFeO_{2.5+\delta}$. This result was expected as enhancement of oxygen up take in perovskites with a tolerance factor close to 1 has been reported from previous exploration of multiple OSMs[85]. As our OSMs are heated beyond their maximum up take temperature, they begin to release oxygen to overcome the concentration gradient established due to oxygen sorption. However, even up to 800 °C in air, the oxygen content does not reach δ = 0 under air flow. This can only be accomplished by reducing the partial pressure of O_2 by switching to N_2. However, the oxidation profile of $Ba_{0.83}Sr_{0.17}FeO_{2.5+\delta}$ resembles our previous work of $Sr_{0.75}Ca_{0.25}FeO_{2.5+\delta}$ and $Sr_{0.7}Ca_{0.3}FeO_{2.5+\delta}$, with a sharp drop in oxygen content/mass at approximately 450 °C. These two $Sr_{1-x}Ca_xFeO_{3-\delta}$ OSMs are among the most promising of the $Sr_{1-x}Ca_xFeO_{3-\delta}$ systems, as this oxygen lability at moderate temperatures led to an increase in desorption kinetics[24]. Recently, Bektas et al.[33] demonstrated the viability of $Ba_{0.75}Sr_{0.25}FeO_{3-\delta}$ as an OSM when implemented in pressure-swing (0.2-0.01 atm O_2), temperature-swing (400-600 °C), and combination processes. Given the difficulties posed by oxidation at higher temperatures in their work, we chose to focus on a purely pressure swing (0.21-0 atm O_2) process at T < 400 °C, at which the oxidation and desorption are near their maximum thermodynamically.

While δ is a useful metric towards understanding the structural changes in these oxygen carriers, oxygen storage is more applied quantity which is traditionally reported in wt.% as a quantification of oxygen produced. The systems in this work containing Ba^{2+}/Sr^{2+} *A*-site compositions are at an inherent disadvantage to Sr^{2+}/Ca^{2+} *A*-site systems due to their higher formula weights. Herein, we compare $Ba_{1-x}Sr_xFeO_{3-\delta}$ (x = 0-0.5) with $SrFeO_{3-\delta}$ and our previously reported $Sr_{0.7}Ca_{0.3}FeO_{3-\delta}$ at 325 °C and 350 °C (Fig. 11). The OSC values for these materials at 325 °C and 350 °C are listed in Table S5. The OSC of $SrFeO_3$ decreases with temperature, while that of $Sr_{0.75}Ca_{0.25}FeO_3$ increases and $Ba_{1-x}Sr_xFeO_{3-\delta}$ OSMs peak at ~350 °C and with a slight shift towards higher temperatures as Sr concentration increases.

At 325 °C, the overall oxygen storage capacities of the studied OSMs are low, with $SrFeO_{3-\delta}$ offering a maximum OSC of 0.93 wt.% over the 60-minute reduction/oxidation cycles. $Ba_{0.83}Sr_{0.17}FeO_{3-\delta}$ and $Ba_{0.75}Sr_{0.25}FeO_{3-\delta}$ are close with 0.88 wt.% and 0.79 wt.%, respectively. However, the initial rate of reduction (oxygen release) is much higher for $SrFeO_3$ than those two OSMs, releasing 0.032 wt.% in the first minute, compared to 0.020 wt.% and 0.012 wt.%, respectively. This initial rate of reduction carries forward through the entire reduction half of the cycle, with the maximum OSC only reached at the 60-minute mark, whereas $SrFeO_{3-\delta}$ is near its equilibrium state after only ~40 minutes. The overall OSC decreases as Sr^{2+} increases from x = 0.17-0.5, with x = 0.08 lagging well behind. Oxidation (oxygen up take) is performed fastest by $Ba_{0.5}Sr_{0.5}FeO_3$ and $SrFeO_3$, although all $Ba_{1-x}Sr_xFeO_{3-\delta}$ with x ≥ 0.17 were much faster than $BaFeO_{3-\delta}$ or $Ba_{0.92}Sr_{0.08}FeO_{3-\delta}$, signaling the importance of the cubic phase.

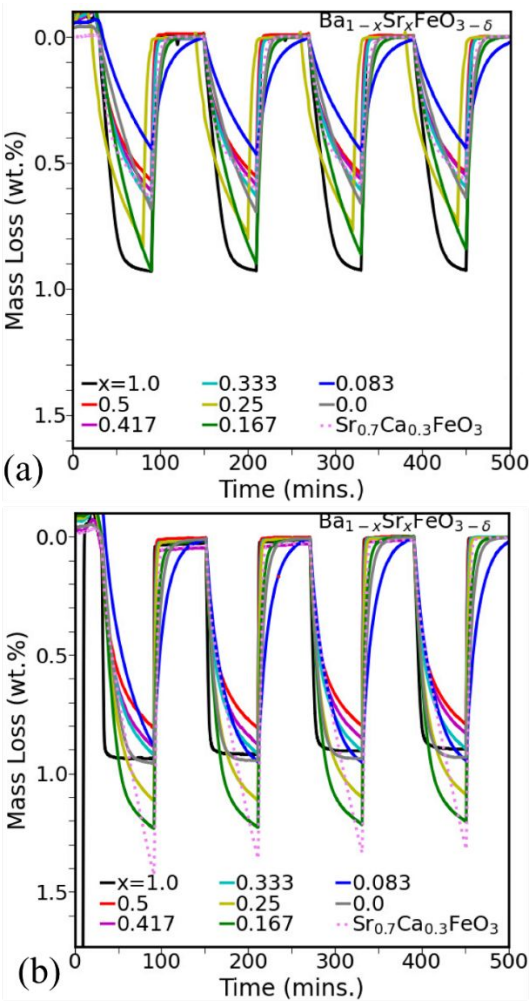

Fig 11. Isothermal TGA oxidation/reduction curves of $Ba_{1-x}Sr_xFeO_{3-\delta}$ (x = 0.0, 0.08, 0.17, 0.25, 0.33, 0.42, 0.50, and 1.0) OSMs at (a) 325 °C, and (b) 350 °C. The oxidation and reduction gas stream are air and N_2, respectively flowing at 75 standard cubic centimeters per minute (sccm). The y-axis is in reverse order to depict positive value for mass loss. The 0 % weight loss represents the weight % of the reversibly accessed oxidized species. A correction factor is taken to align the plots with the maximum oxidation at 0 to show mass gain. The results for $Sr_{0.7}Ca_{0.3}FeO_{3-\delta}$ OSMs are shown for comparison purposes. Four total Air/N_2 cycles were performed to gauge initial stability.

Unlike 325 °C, the beneficial effects of $Ba_{1-x}Sr_xFeO_{3-\delta}$ versus $SrFeO_{3-\delta}$ are observed at 350 °C (Fig. 11b). While $Sr_{0.7}Ca_{0.3}FeO_{3-\delta}$ has the highest OSC over the 60-minute reduction cycle (1.32 wt.%), its overall reduction rate (0.041 wt.%) is lower than every other OSM tested, except $Ba_{0.92}Sr_{0.08}FeO_{3-\delta}$. Conversely, the initial reduction rate (0.145 wt.%/min) is still dominated by $SrFeO_{3-\delta}$ at 350 °C , but its OSC (0.90 wt.%) is lower than at 325 °C. This trend is commonly observed in OSMs operating above the temperature of maximum oxygen release, observable by O_2-TPD (Fig. 9). Unlike $SrFeO_3$, every other tested OSM shows an increase in OSC at 350 °C compared to 325 °C. In fact, $Ba_{0.83}Sr_{0.17}FeO_{3-\delta}$ and $Ba_{0.75}Sr_{0.25}FeO_{3-\delta}$ offer attractive compromises between $Sr_{0.7}Ca_{0.3}FeO_{3-\delta}$ and $SrFeO_{3-\delta}$, with OSCs of 1.21% or 1.10% and initial reduction rates of 0.070%/min and 0.092 wt.%/min, respectively. Between a reduction time of 16-50 minutes, these two OSMs are the most preferred for the reduction. Between those two $Ba_{1-x}Sr_xFeO_{3-\delta}$ OSMs, the initial oxidation rates over the first minute are faster for x = 0.25 (0.35 wt.%/min vs. 0.24 wt.%/min). Both are slower than $SrFeO_{3-\delta}$ (0.54 wt.%/min) and faster than $Sr_{0.7}Ca_{0.3}FeO_{3-\delta}$ (0.13 wt.%/min). However, full reoxidation of $Ba_{0.83}Sr_{0.17}FeO_{3-\delta}$ does take approximately 6 minutes longer than $Sr_{0.7}Ca_{0.3}FeO_{3-\delta}$ (17 vs. 11 minutes). Only $BaFeO_3$ and $Ba_{0.92}Sr_{0.08}FeO_3$ have slower oxidation profiles, further confirming the importance of the cubic structure versus hexagonal to yield the most favorable reaction kinetics, in agreement with the findings by Watanabe, et al [46]. A table summarizing the OSC, oxidation, and reduction rates for all the OSMs studied in this work are in Table S5.

While the oxygen storage activity of selected $Ba_{1-x}Sr_xFeO_{3-\delta}$ OSMs can compete well with both $SrFeO_{3-\delta}$ and $Sr_{1-x}Ca_xFeO_{3-\delta}$, the true strength of those two systems is the compositional variability that can be modulated further using *A*-site or *B*-site substitution, or a combination of both. Initial reports on the limits and feasibility of the $Ba_{1-x}Sr_xFeO_{3-\delta}$ family of OSMs suggest that while Mg^{2+} *B*-site substitution has shown to enhance the oxidation kinetics of these materials[33], further substitution remains unexplored. We believe that cubic $Ba_{1-x}Sr_xFeO_{3-\delta}$ offers a promising foundation for investigation into *A*-/*B*-site substitution or microstructural modifications, particularly for applications at low operating temperatures, especially below 400 °C. Other perovskites such as $Sr_{1-x}Ca_xFeO_3$ often reach their lower temperature limits at approximately 375 °C, unless Co is added, which may pose socio-economic challenges for widespread implementation of the CLAS technology. Minor improvements to $Ba_{1-x}Sr_xFeO_{3-\delta}$, either through compositional adjustments or increased surface area, could potentially lead to a new promising class of sub-400 °C OSMs.

Conclusions

In this study, we utilize the DFT-based energy analysis and XRD measurements to demonstrate that the crystal phase of the $Ba_{1-x}Sr_xFeO_{3-\delta}$ perovskites can be manipulated by varying Sr concentration, resulting in either a hexagonal or cubic phase. The atomistic models of the base $BaFeO_{3-\delta}$ and mixed $Ba_{1-x}Sr_xFeO_{3-\delta}$ perovskites are developed and the preferred oxygen vacancy formation sites are identified within the hexagonal (12*H*, 6*H*), and cubic 3*C* phases. The cubic phase based $Ba_{1-x}Sr_xFeO_{3-\delta}$ perovskites exhibit lower oxygen vacancy formation energy compared to their hexagonal counterparts. Additionally, their thermodynamic stability and spontaneous oxidizing properties make them promising oxygen storage materials. The electronic structure in terms of Fe-3*d* and O-2*p* hybridization serves as a descriptor for the thermodynamic cost to create an oxygen vacancy. The high and stable redox performance of the $Ba_{0.75}Sr_{0.25}FeO_3$ perovskite at 325 °C and 350 °C establish it as a promising OSM for low-temperature chemical looping air

separation technology. The enhanced low-temperature OSC of $Ba_{1-x}Sr_xFeO_{3-\delta}$ perovskites, computationally identified as having the lowest redox thermodynamics, highlight the importance of such analysis in advancing the development of mixed perovskite with improved thermal OSC capabilities as required for low temperature chemical looping applications. The aspects presented in this study provide valuable insights for improving the performance of OSMs and advancing energy-efficient O_2 production.

Disclaimer

This project was funded by the United States Department of Energy, National Energy Technology Laboratory, in part, through a site support contract. Neither the United States Government nor any agency thereof, nor any of their employees, nor the support contractor, nor any of their employees, makes any warranty, express or implied, or assumes any legal liability or responsibility for the accuracy, completeness, or usefulness of any information, apparatus, product, or process disclosed, or represents that its use would not infringe privately owned rights. Reference herein to any specific commercial product, process, or service by trade name, trademark, manufacturer, or otherwise does not necessarily constitute or imply its endorsement, recommendation, or favoring by the United States Government or any agency thereof. The views and opinions of authors expressed herein do not necessarily state or reflect those of the United States Government or any agency thereof.

Author contributions

S. R. A. conceived the concepts of this work, designed, and performed the computational work, analysed the data and prepared the manuscript. E.J.P. synthesized the samples, performed TGA measurements and wrote the experimental sections of the manuscript. H.P.P. analysed the data, S.N. performed the O_2-TPD measurements. J. W.L. and Y.D. supervised the work.

Conflicts of interest

There are no conflicts to declare.

Data availability

The data supporting this article have been included as part of the Supplementary Information. Further data are available upon request from the authors.

Acknowledgements

This work was performed in support of the U.S. Department of Energy's (DOE) Fossil Energy and Carbon Management's Gasification Program and executed through the National Energy Technology Laboratory (NETL) Research & Innovation Center's Advanced Reaction Systems Field Work Proposal. We acknowledge the Joule supercomputer at National Energy Technology Laboratory for computational resources.

References

1 T.-Z. Ang, M. Salem, M. Kamarol, H. S. Das, M. A. Nazari and N. Prabaharan, A comprehensive study of renewable energy sources: Classifications, challenges and suggestions, *Energy Strategy Reviews*, 2022, **43**, 100939.

2 X. Wang and C. Song, Carbon Capture From Flue Gas and the Atmosphere: A Perspective, *Front. Energy Res.*, 2020, **8**, 560849.

3 S. Arrhenius, On the Influence of Carbonic Acid in the Air upon the Temperature of the Ground, *Philosophical Magazine and Journal of Science*, 1896, **41**, 237-276.

4 B. J. P. Buhre, L. K. Elliott, C. D. Sheng, R. P. Gupta and T. F. Wall, Oxy-fuel combustion technology for coal-fired power generation, *Progress in Energy and Combustion Science*, 2005, **31**, 283–307.

5 R. Daiyan, E. C. Lovell, B. Huang, M. Zubair, J. Leverett, Q. Zhang, S. Lim, J. Horlyck, J. Tang, X. Lu, K. Kalantar-Zadeh, J. N. Hart, N. M. Bedford and R. Amal, Uncovering Atomic-Scale Stability and Reactivity in Engineered Zinc Oxide Electrocatalysts for Controllable Syngas Production, *Advanced Energy Materials*, 2020, **10**, 2001381.

6 I. Pfaff and A. Kather, Comparative thermodynamic analysis and integration issues of CCS steam power plants based on oxy-combustion with cryogenic or membrane based air separation, *Energy Procedia*, 2009, **1**, 495–502.

7 T. Banaszkiewicz, M. Chorowski and W. Gizicki, Comparative analysis of cryogenic and PTSA technologies for systems of oxygen production, *AIP Conference Proceeding*, 2014, **1573**, 1373–137.

8 V. V. Belousov and S. V. Fedorov, An Oxygen-Permeable Bilayer MIEC-Redox Membrane Concept, *ACS Appl. Mater. Interfaces*, 2018, **10**, 21794–21798.

9 B. Moghtaderi, Application of Chemical Looping Concept for Air Separation at High Temperatures †, *Energy Fuels*, 2010, **24**, 190–198.

10 A. R. Smith and J. Klosek, A review of air separation technologies and their integration with energy conversion processes, *Fuel Processing Technology*, 2001, **70**, 115–134.

11 Warren K. Lewis, Newton, and Edwin R. Gilliland, Production of Pure Carbon Dioxide, United States Patent Office, 1954, patent number 2665972.

12 T. Mattisson, A. Lyngfelt and H. Leion, Chemical-looping with oxygen uncoupling for combustion of solid fuels, *International Journal of Greenhouse Gas Control*, 2009, **3**, 11–19.

13 Q. Imtiaz, D. Hosseini and C. R. Müller, Review of Oxygen Carriers for Chemical Looping with Oxygen Uncoupling (CLOU): Thermodynamics, Material Development, and Synthesis, *Energy Tech*, 2013, **1**, 633–647.

14 J. Dou, E. Krzystowczyk, X. Wang, T. Robbins, L. Ma, X. Liu and F. Li, A- and B-site Codoped $SrFeO_3$ Oxygen Sorbents for Enhanced

Chemical Looping Air Separation, *ChemSusChem*, 2020, **13**, 385–393.

15 E. Krzystowczyk, V. Haribal, J. Dou and F. Li, Chemical Looping Air Separation Using a Perovskite-Based Oxygen Sorbent: System Design and Process Analysis, *ACS Sustainable Chem. Eng.*, 2021, **9**, 12185–12195.

16 P. K. Gallagher, J. B. MacChesney and D. N. E. Buchanan, Mössbauer Effect in the System SrFeO2.5–3.0, *The Journal of Chemical Physics*, 1964, **41**, 2429–2434.

17 J. B. MacChesney, J. J. Jetzt, J. F. Potter, H. J. Williams and R. C. Sherwood, Electrical and Magnetic Properties of the System $SrFeO_3$–$BiFeO_3$, *Journal of the American Ceramic Society*, 1966, **49**, 644–647.

18 T. Ferreira, S. R. Acharya, Y. W. Li, D. S. Parker, A. S. Sefat and V. R. Cooper, Unintended consequence of topochemical reduction of $SrFeO_3$ to $SrFeO_2$: Design of infinite layered oxides, *Phys. Rev. Materials*, 2021, **5**, 123401.

19 N. Galinsky, A. Mishra, J. Zhang and F. Li, $Ca_{1-x}A_xMnO_3$ (A = Sr and Ba) perovskite based oxygen carriers for chemical looping with oxygen uncoupling (CLOU), *Applied Energy*, 2015, **157**, 358–367.

20 A. Mishra, T. Li, F. Li and E. E. Santiso, Oxygen Vacancy Creation Energy in Mn-Containing Perovskites: An Effective Indicator for Chemical Looping with Oxygen Uncoupling, *Chem. Mater.*, 2019, **31**, 689–698.

21 C. Y. Lau, M. T. Dunstan, W. Hu, C. P. Grey and S. A. Scott, Large scale in silico screening of materials for carbon capture through chemical looping, *Energy Environ. Sci.*, 2017, **10**, 818–831.

22 B. Bulfin, J. Lapp, S. Richter, D. Gubàn, J. Vieten, S. Brendelberger, M. Roeb and C. Sattler, Air separation and selective oxygen pumping via temperature and pressure swing oxygen adsorption using a redox cycle of SrFeO3 perovskite, *Chemical Engineering Science*, 2019, **203**, 68–75.

23 N. Miura, H. Ikeda and A. Tsuchida, $Sr_{1-x}Ca_xFeO_{3-\delta}$ as a New Oxygen Sorbent for the High-Temperature Pressure-Swing Adsorption Process, *Ind. Eng. Chem. Res.*, 2016, **55**, 3091–3096.

24 E. J. Popczun, D. N. Tafen, S. Natesakhawat, C. M. Marin, T.-D. Nguyen-Phan, Y. Zhou, D. Alfonso and J. W. Lekse, Temperature tunability in $Sr_{1-x}Ca_xFeO_{3-\delta}$ for reversible oxygen storage: a computational and experimental study, *J. Mater. Chem. A*, 2020, **8**, 2602–2612.

25 T. Jia, E. J. Popczun, J. W. Lekse and Y. Duan, Effective Ca^{2+}-doping in $Sr_{1-x}Ca_xFeO_{3-\delta}$ oxygen carriers for chemical looping air separation: A theoretical and experimental investigation, *Applied Energy*, 2021, **281**, 116040.

26 J. Dou, E. Krzystowczyk, X. Wang, A. R. Richard, T. Robbins and F. Li, $Sr_{1-x}Ca_xFe_{1-y}Co_yO_{3-\delta}$ as facile and tunable oxygen sorbents for chemical looping air separation, *J. Phys. Energy*, 2020, **2**, 025007.

27 E. J. Popczun, T. Jia, S. Natesakhawat, C. M. Marin, T. Nguyen-Phan, Y. Duan and J. W. Lekse, Investigation of $Sr_{0.7}Ca_{0.3}FeO_3$ Oxygen Carriers with Variable Cobalt B-Site Substitution, *ChemSusChem*, 2021, **14**, 1893–1901.

28 E. J. Popczun, T. Jia, S. Natesakhawat, W. Xu, C. M. Marin, Y. Duan and J. W. Lekse, Nickel B-site substitution in bulk $Sr_{1-x}Ca_xFeO_3$ perovskite oxygen carriers: Benefits and limitations, *Journal of Alloys and Compounds*, 2022, **896**, 162783.

29 B. A. Duell, A. Ramazani, S. Natesakhawat, E. J. Popczun, J. W. Lekse and Y. Duan, Targeted Chemical Looping Materials Discovery by an Inverse Design, *Advanced Intelligent Systems*, 2025, 2401118.

30 S. Ogawa, S. Tamura, H. Yamane, T. Tanabe, M. Saito and T. Motohashi, New Triclinic Perovskite-Type Oxide $Ba_5CaFe_4O_{12}$ for Low-Temperature Operated Chemical Looping Air Separation, *J. Am. Chem. Soc.*, 2023, **145**, 22788–22795.

31 Z. Zhang, L. Andre and S. Abanades, Experimental assessment of oxygen exchange capacity and thermochemical redox cycle behavior of Ba and Sr series perovskites for solar energy storage, *Solar Energy*, 2016, **134**, 494–502.

32 H. E. Bush, M. Kury, Z. Berquist, T. Rivas, M. Finale, K. Albrecht and A. Ambrosini, Air separation and N_2 purification with $Ba_{0.15}Sr_{0.85}FeO_{3-\delta}$ via a two-step thermochemical process, *Solar Energy*, 2024, **268**, 112268.

33 H. Bektas, R. Cai, L. Brody and F. Li, Structural and Thermodynamic Assessment of Ba and Ba/Mg Substituted $SrFeO_{3-\delta}$ for "Low-Temperature" Chemical Looping Air Separation, *Energy Fuels*, 2024, **38**, 11107–11118.

34 A. R. P. Harrison, K. Y. Kwong, Y. Zheng, A. Balkrishna, A. Dyson and E. J. Marek, Kinetic and Thermodynamic Enhancement of Low-Temperature Oxygen Release from Strontium Ferrite Perovskites Modified with Ag and CeO_2, *Energy Fuels*, 2023, **37**, 9487–9499.

35 E. J. Popczun, S. Natesakhawat, C. M. Marin, J. Riley, B. A. Duell and J. W. Lekse, Porosity in $Sr_{1-x}Ca_xFeO_{3-\delta}$ oxygen carriers: The role of surface area and pretreatment on storage activity, *Journal of Alloys and Compounds*, 2024, **979**, 173526.

36 T. Jia, E. J. Popczun, J. W. Lekse and Y. Duan, The optimal co-doping of $SrFe_{1-x}Co_xO_{3-\delta}$ oxygen carriers in redox applications, *Phys. Chem. Chem. Phys.*, 2020, **22**, 16721–16726.

37 T. Jia, J. W. Lekse, G. A. Hackett and Y. Duan, Effects of Site and Magnetic Disorder on the Oxygen Vacancy Formation and Electronic and Optical Properties of $La_xSr_{1-x}CoO_{3-\delta}$ and $SrFe_yCo_{1-y}O_{3-\delta}$, *J. Phys. Chem. C*, 2021, **125**, 12374–12381.

38 A. Ramazani, B. A. Duell, E. J. Popczun, S. Natesakhawat, T. Nandi, J. W. Lekse and Y. Duan, High-throughput ab initio calculations and machine learning to discover $SrFeO_3$-based perovskites for chemical-looping applications, *Cell Reports Physical Science*, 2024, **5**, 101797.

39 E. Krzystowczyk, X. Wang, J. Dou, V. Haribal and F. Li, Substituted $SrFeO_3$ as robust oxygen sorbents for thermochemical air separation: correlating redox performance with compositional and structural properties, *Phys. Chem. Chem. Phys.*, 2020, **22**, 8924–8932.

40 M. F. Hoedl, D. Gryaznov, R. Merkle, E. A. Kotomin and J. Maier, Interdependence of Oxygenation and Hydration in Mixed-Conducting (Ba,Sr)$FeO_{3-\delta}$ Perovskites Studied by Density Functional Theory, *J. Phys. Chem. C*, 2020, **124**, 11780–11789.

41 A. Rahmani, K. Driss Khodja and B. Amrani, Mechanical Stability, Magnetic and Electronic Properties of $Sr_{1-x}Ba_xFeO_3$: DFT+U Study, *Acta Phys. Pol. A*, 2020, **138**, 469–476.

42 G. He, S. Baumann, F. Liang, H. Hartmann, H. Jiang and W. A. Meulenberg, Phase stability and oxygen permeability of Fe-based $BaFe_{0.9}Mg_{0.05}X_{0.05}O_3$ (X = Zr, Ce, Ca) membranes for air separation, *Separation and Purification Technology*, 2019, **220**, 176–182.

43 M. Pouchard, J.-C. Grenier, A. Wattiaux, and P. Hagenmuller, On the $BaFeO_{3-y}$ system ($0 < y \leq 0.5$), Journal of Solid state chemistry, 1989, **80**, 6-11.

44 T. Takeda, Y. Yamaguchi, and H. Watanabe, J. Phys. Soc. Jpn. 33, 967 (1972).

45 Z. Tan, F. Denis Romero, T. Saito, M. Goto, M. Amano Patino, A. Koedtruad, Y. Kosugi, W.-T. Chen, Y.-C. Chuang, H.-S. Sheu, J. P. Attfield and Y. Shimakawa, Charge disproportionation and interchange transitions n twelve-layer $BaFeO_3$, *Phys. Rev. B*, 2020, **102**, 054404.

46 R. Watanabe, M. Goto, Y. Kosugi, D. Kan and Y. Shimakawa, Oxygen Release and Incorporation Behaviors in $BaFeO_3$ Polymorphs with Unusually High-Valence Fe^{4+}, *Chem. Mater.*, 2024, **36**, 2106–2112.

47 T. Jia, Z. Zeng, X. Zhang, P. Ohodnicki, B. Chorpening, G. Hackett, J. Lekse and Y. Duan, The influence of oxygen vacancy on the electronic and optical properties of $ABO_{3-\delta}$ (A = La, Sr, B = Fe, Co) perovskites, *Phys. Chem. Chem. Phys.*, 2019, **21**, 20454–20462.

48 T. Jia, J. Lekse and Y. Duan, Effect of Multiple Oxygen Vacancies on the Optical and Thermodynamic Properties of $La_{0.75}Sr_{0.25}Co_{0.25}Fe_{0.75}O_{3-\delta}$ Perovskite, *J. Phys. Chem. C*, 2022, **126**, 11421–11425.

49 P. Hohenberg and W. Kohn, Inhomogeneous Electron Gas, *Phys. Rev.*, 1964, **136**, B864–B871.

50 W. Kohn and L. J. Sham, Self-Consistent Equations Including Exchange and Correlation Effects, *Phys. Rev.*, 1965, **140**, A1133–A1138.

51 G. Kresse and J. Furthmüller, Efficiency of ab-initio total energy calculations for metals and semiconductors using a plane-wave basis set, *Computational Materials Science*, 1996, **6**, 15–50.

52 P. E. Blöchl, Projector augmented-wave method, *Phys. Rev. B*, 1994, **50**, 17953–17979.

53 G. Kresse and D. Joubert, From ultrasoft pseudopotentials to the projector augmented-wave method, *Phys. Rev. B*, 1999, **59**, 1758–1775.

54 J. P. Perdew, A. Ruzsinszky, G. I. Csonka, O. A. Vydrov, G. E. Scuseria, L. A. Constantin, X. Zhou and K. Burke, Restoring the Density-Gradient Expansion for Exchange in Solids and Surfaces, *Phys. Rev. Lett.*, 2008, **100**, 136406.

55 H. J. Monkhorst and J. D. Pack, Special points for Brillouin-zone integrations, *Phys. Rev. B*, 1976, **13**, 5188–5192.

56 S. L. Dudarev, G. A. Botton, S. Y. Savrasov, C. J. Humphreys and A. P. Sutton, Electron-energy-loss spectra and the structural stability of nickel oxide: An LSDA+U study, *Phys. Rev. B*, 1998, **57**, 1505–1509.

57 B. Ribeiro, M. Godinho, C. Cardoso, R. P. Borges and T. P. Gasche, Self-doping and the role of oxygen vacancies in the magnetic properties of cubic $BaFeO_{3-\delta}$, *Journal of Applied Physics*, 2013, **113**, 083906.

58 G. Henkelman, B. P. Uberuaga and H. Jónsson, A climbing image nudged elastic band method for finding saddle points and minimum energy paths, *The Journal of Chemical Physics*, 2000, **113**, 9901–9904.

59 A. Togo and I. Tanaka, First principles phonon calculations in materials science, *Scripta Materialia*, 2015, **108**, 1–5.

60 J. B. MacChesney, J. F. Potter, R. C. Sherwood and H. J. Williams, Oxygen Stoichiometry in the Barium Ferrates; Its Effect on Magnetization and Resistivity, *The Journal of Chemical Physics*, 1965, **43**, 3317–3322.

61 I. Gil De Muro, M. Insausti, L. Lezama and T. Rojo, Effect of the synthesis conditions on the magnetic and electrical properties of the $BaFeO_{3-x}$ oxide: A metamagnetic behavior, *Journal of Solid State Chemistry*, 2005, **178**, 1712–1719.

62 O. Clemens, R. Haberkorn, P. R. Slater and H. P. Beck, Synthesis and characterisation of the $Sr_xBa_{1-x}FeO_{3-y}$-system and the fluorinated phases $Sr_xBa_{1-x}FeO_2F$, *Solid State Sciences*, 2010, **12**, 1455–1463.

63 D. Gutiérrez-Martín, A. Varela, M. Hernando, A. Torres-Pardo, E. Matesanz, I. Gómez-Recio, J. M. González-Calbet, M. T. Fernández-Díaz, J. J. Calvino, M. A. Cauqui, M. P. Yeste and M. Parras, Exploring Reversible Redox Behavior in the 6H-$BaFeO_{3-\delta}$ ($0 < \delta < 0.4$) System: Impact of Fe^{3+}/Fe^{4+} Ratio on CO Oxidation, *Inorg. Chem.*, 2024, **63**, 8908–8918.

64 Y. Suga, M. Hibino, T. Kudo and N. Mizuno, Electrochemical Oxidation of $BaFeO_{2.5}$ to $BaFeO_3$, *Electrochimica Acta*, 2014, **137**, 359–362.

65 N. Hayashi, T. Yamamoto, H. Kageyama, M. Nishi, Y. Watanabe, T. Kawakami, Y. Matsushita, A. Fujimori and M. Takano, $BaFeO_3$: A Ferromagnetic Iron Oxide, *Angew Chem Int Ed*, 2011, **50**, 12547–12550.

66 W. A. Adeagbo, I. V. Maznichenko, H. Ben Hamed, I. Mertig, A. Ernst and W. Hergert, Electronic and Magnetic Properties of $BaFeO_3$ on the Pt(111) Surface in a Quasicrystalline Approximant Structure, *Physica Status Solidi (b)*, 2020, **257**, 1900649.

67 Y. Takeda, M. Shimada, F. Kanamaru and M. Koizumi, Synthesis of 12-layer modification of hexagonal $BaFeO_3$ under high oxygen pressure, *Journal of Solid State Chemistry*, 1973, **7**, 229–231.

68 S. Mori, Phase Transformation in Barium Orthoferrate, $BaFeO_{3-x}$, *Journal of the American Ceramic Society*, 1966, **49**, 600–605.

69 K. Mori, T. Kamiyama, H. Kobayashi, K. Oikawa, T. Otomo and S. Ikeda, Structural Evidence for the Charge Disproportionation of Fe^{4+} in $BaFeO_{3-\delta}$, *J. Phys. Soc. Jpn.*, 2003, **72**, 2024–2028.

70 M. F. Hoedl, C. Ertural, R. Merkle, R. Dronskowski and J. Maier, The Orbital Nature of Electron Holes in $BaFeO_3$ and Implications for Defect Chemistry, *J. Phys. Chem. C*, 2022, **126**, 12809–12819.

71 T. Tsuyama, T. Matsuda, S. Chakraverty, J. Okamoto, E. Ikenaga, A. Tanaka, T. Mizokawa, H. Y. Hwang, Y. Tokura and H. Wadati, X-ray spectroscopic study of $BaFeO_3$ thin films: An Fe^{4+} ferromagnetic insulator, *Phys. Rev. B*, 2015, **91**, 115101.

72 I. V. Maznichenko, S. Ostanin, L. V. Bekenov, V. N. Antonov, I. Mertig and A. Ernst, Impact of oxygen doping and oxidation state of iron on the electronic and magnetic properties of $BaFeO_{3-\delta}$, *Phys. Rev. B*, 2016, **93**, 024411.

73 I. Cherair, E. Bousquet, M. M. Schmitt, N. Iles and A. Kellou, First-principles study of strain-induced Jahn–Teller distortions in $BaFeO_3$, *J. Phys.: Condens. Matter*, 2018, **30**, 255701.

74 M. Parras, M. Vallet-Regi, J. M. Gonzalez-Calbet, J. C. Grenier, P. Hagenmuller and J. Rodriguez-Carvajal, ChemInform Abstract: A Structural Study of 12H-$BaFeO_{2.93}$, *ChemInform*, 1989, **20**, chin.198950010.

75 M. Parras, M. Vallet-Regi, J. M. Gonzalez-Calbet and J. C. Grenier, Journal of Solid State Chemistry, 1989, **83**, 121-131.

76 D. Juan, M. Pruneda and V. Ferrari, Localized electronic vacancy level and its effect on the properties of doped manganites, *Sci Rep*, 2021, **11**, 6706.

77 H. Guo, J. Wang, X. He, Z. Yang, Q. Zhang, K. Jin, C. Ge, R. Zhao, L. Gu, Y. Feng, W. Zhou, X. Li, Q. Wan, M. He, C. Hong, Z. Guo, C. Wang, H. Lu, K. Ibrahim, S. Meng, H. Yang and G. Yang, The Origin of Oxygen Vacancies Controlling $La_{2/3}Sr_{1/3}MnO_3$ Electronic and Magnetic Properties, *Adv Materials Inter*, 2016, **3**, 1500753.

78 A. E. Hadri, I. Gómez-Recio, E. D. Río, J. C. Hernández-Garrido, R. Cortés-Gil, M. Hernando, Á. Varela, Á. Gutiérrez-Alonso, M. Parras, J. J. Delgado, J. A. Pérez-Omil, G. Blanco, J. J. Calvino and J. M. González-Calbet, Critical Influence of Redox Pretreatments on the CO Oxidation Activity of $BaFeO_{3-\delta}$ Perovskites: An in-Depth Atomic-Scale Analysis by Aberration-Corrected and in Situ Diffraction Techniques, *ACS Catal.*, 2017, **7**, 8653–8663.

79 E. Lucchini, S. Meriani and D. Minichelli, An X-ray study of two phases of $BaFeO_{3-x}$, *Acta Crystallogr B Struct Crystallogr Cryst Chem*, 1973, **29**, 1217–1219.

80 Y. Hinuma, S. Mine, T. Toyao and K. Shimizu, Trends in Surface Oxygen Formation Energy in Perovskite Oxides, *ACS Omega*, 2022, **7**, 18427–18433.

81 V. M. Goldschmidt, Die Gesetze der Krystallochemie, *Naturwissenschaften*, 1926, **14**, 477–485.

82 S. R. Acharya, S. I. Shah and T. S. Rahman, Diffusion of small Cu islands on the Ni(111) surface: A self-learning kinetic Monte Carlo study, *Surface Science*, 2017, **662**, 42–58.

83 O. Clemens, M. Gröting, R. Witte, J. M. Perez-Mato, C. Loho, F. J. Berry, R. Kruk, K. S. Knight, A. J. Wright, H. Hahn and P. R. Slater, Crystallographic and Magnetic Structure of the Perovskite-Type Compound $BaFeO_{2.5}$: Unrivalled Complexity in Oxygen Vacancy Ordering, *Inorg. Chem.*, 2014, **53**, 5911–5921.

84 H. J. V. Hook, Oxygen Stoichiometry in the Compound $BaFe0_{3-x}$, *The Journal of Physical Chemistry*, 1964, **68**,3786-3789.

85 T. Masunaga, J. Izumi and N. Miura, Relationship between oxygen sorption properties and crystal structure of Fe-based oxides with double perovskite composition, *Chemical Engineering Science*, 2012, **84**, 108–112.

The data supporting this article have been included as part of the Supplementary Information. Further data are available upon request from the authors.